Supporting Information

Phenothiazine-based anodes with π-conjugation extension and dynamic charge balance enabling ultra-stable hydronium-ion batteries

Yunpeng Zhou, Lintong Hu,* Yongzhihan He, Huilin Wei, Can Cui and Chao Yan*

School of Materials Science and Engineering, Jiangsu University of Science and Technology, Zhenjiang, 212003, P. R. China. E-mail: hulintong2020@just.edu.cn; chaoyan@just.edu.cn

Experimental section

Syntheses of TTA: TTA was synthesized through a dehydration condensation reaction between thionine and hexaketocyclohexane octahydrate ($C_6O_6 \cdot 8H_2O$). In a typical procedure, thionine (0.861 g, 0.3 mmol) and C_6O_6 (0.312 g, 0.1 mmol) were dissolved in acetic acid (120 mL). The resulting solution was subsequently heated to 95 °C and held at this temperature for 24 h. After the solution had cooled down, the precipitate was separated out via centrifugation (8000 rpm, 10 min) and sequentially washed with glacial acetic acid, ethanol, and deionized water to remove unreacted precursors and byproducts. Finally, drying the purified TTA powder at 60 °C for 12 h afforded the desired product.

Electrodepostion of the MnO_2 cathode: A three-electrode system was employed for the electrodeposition of MnO_2, consisting of an Ag/AgCl reference electrode, a graphite rod counter electrode and a piece of graphite felt (1 cm^2 in area) working electrode. The electrolyte was 2 M $MnSO_4$ and 2 M H_2SO_4. MnO_2 was successfully deposited via galvanostatic

electrodeposition at 0.25 mA cm^{-2} for 1 h. Based on equation *It = nZF*, a deposition of 0.25 mAh cm^{-2} corresponds to a mass loading of 0.4 mg cm^{-2}.

Material characterizations*:* Fourier transform infrared spectroscopy (FTIR, Nicolet 6700). X-ray diffraction (XRD, Bruker D2). Scanning electron microscopy (SEM, Nova NanoSem450). ^{1}H nuclear magnetic resonance spectra (^{1}H NMR, German Bruker Ascend TM 600 MHz). Raman spectrum (Renishaw inVIA). Solid-state ^{13}C NMR (Bruker Avance Neo 400WB).

Electrochemical measurements: The electrode slurry was prepared by homogenizing active material TTA, conductive carbon black, and polyvinylidene fluoride in a mass ratio of 6:3:1 using N-methyl pyrrolidone as the solvent. The resulting paste was uniformly coated onto carbon paper and dried under vacuum at 60 °C for 24 h. The active material loading was controlled within 1 mg per electrode. A three-electrode system was employed for the electrochemical evaluation of the anode and cathode, comprising the working electrode (TTA or MnO_2@GF), an Ag/AgCl reference electrode, and a graphite rod counter electrode, with 2 M H_2SO_4 as the electrolyte. The full cell was assembled using TTA as the anode and MnO_2@GF as the cathode, separated by a Nafion 212 membrane to prevent electrolyte crossover. The anodic compartment contained 2 M H_2SO_4, while the catholyte consisted of 2 M H_2SO_4 containing 2 M $MnSO_4$. To maintain capacity balance between the cathode and anode, the mass loading of the TTA electrode was set to approximately 1.8 mg cm^{-2}. All electrochemical measurements, including cyclic voltammetry (CV) and galvanostatic charge-discharge (GCD) tests, were performed on a CHI760E electrochemical workstation.

Calculation of the capacity and energy density: The capacity (*Q*, mAh g^{-1}) of the TTA electrode is calculated according to the following equation:

$$Q = \frac{I_{dis} \times t_{dis}}{m_{TTA}}$$

where I_{dis} (mA) is the discharge current, t_{dis} is the discharge time, and m_{TTA} is the mass of TTA. The energy density (E, Wh kg^{-1}) of the full cell is calculated according to the following equation:

$$E = \frac{\int_{t1}^{t2} I_{dis} \times V dt}{m_{total}}$$

, where *t1* (s) and *t2* (s) are the discharge starting and ending time, I_{dis} (mA) is the discharge current, V (V) is the voltage window, and m_{total} is the total mass of the active materials for both the anode and cathode.

Theoretical calculation

Density functional theory (DFT) calculations were carried out using the Gaussian 09W software package to obtain structural characteristics of oxidized and reduced molecular forms. For the geometrical optimization process, the B3LYP/6-31G(d) basis set was employed. Taking the optimized molecular structures as the foundation, we visualized the results of HOMO/LUMO and electrostatic potential (ESP) analyses with Gaussview 5.0 software.

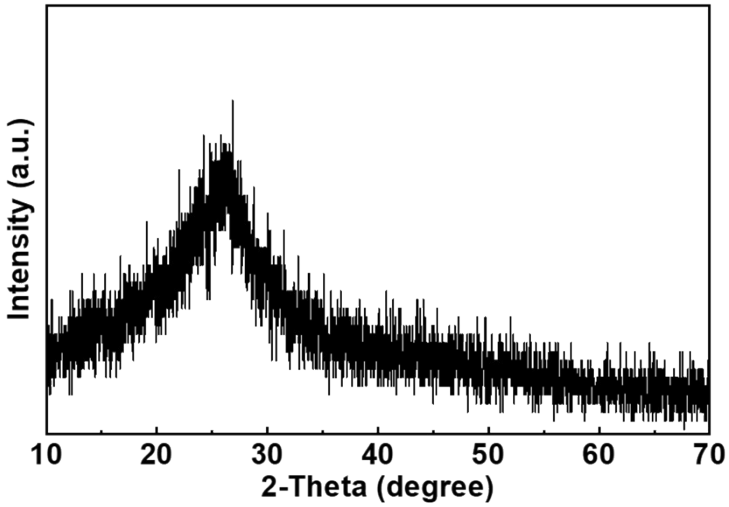

Figure S1. XRD pattern of the TTA powder.

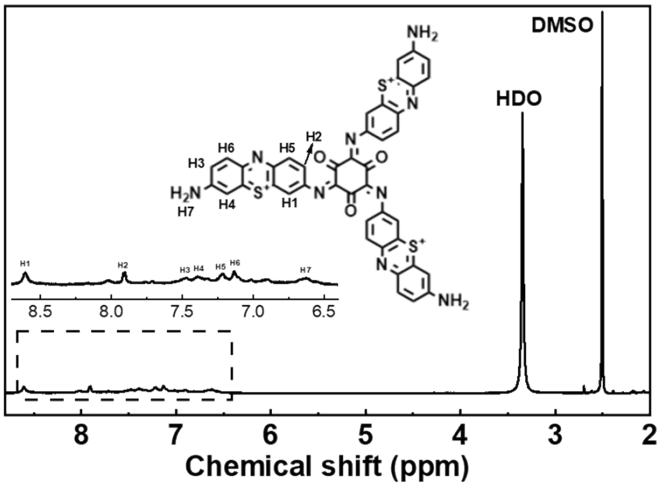

Figure S2. ^{1}H NMR spectrum (600 MHz, DMSO-d6) of TTA sample.

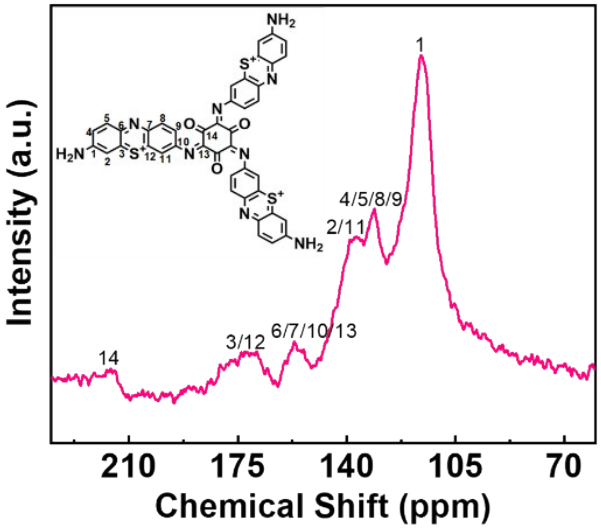

Figure S3. Solid-state ^{13}C NMR of spectrum of TTA.

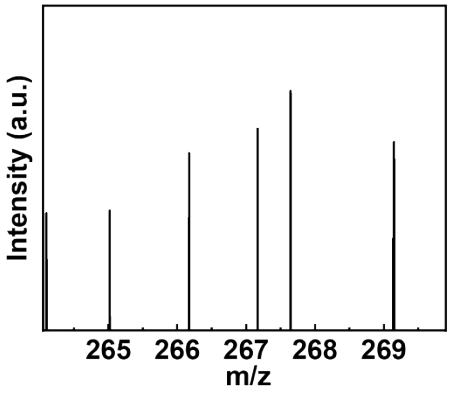

Figure S4. Mass spectrum of TTA.

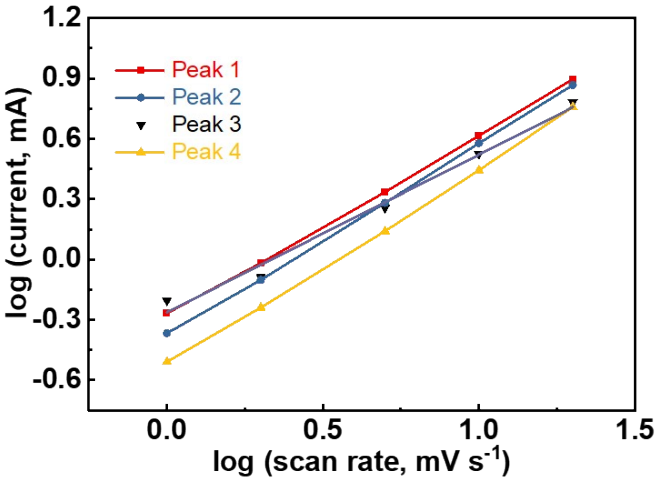

Figure S5. The relationship of peak current with the scan rate from CV curves.

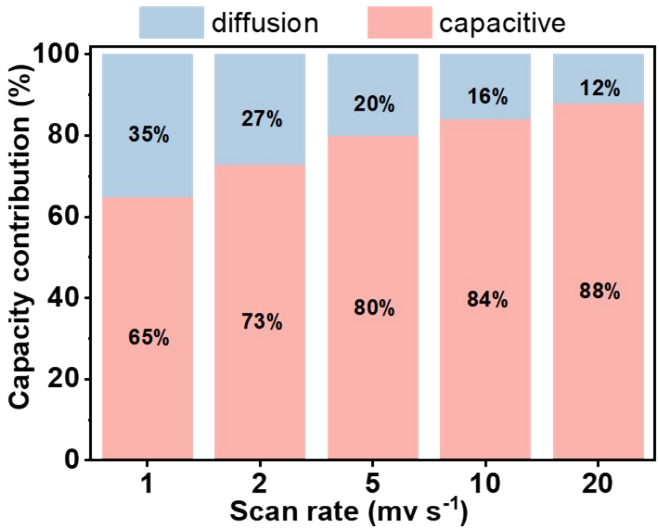

Figure S6. The capacitive and diffusive capacity contributions at different current densities.

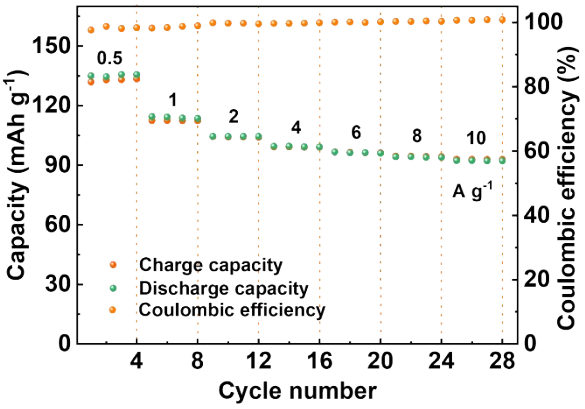

Figure S7. Rate performance of the TTA electrode in H_2SO_4 electrolyte.

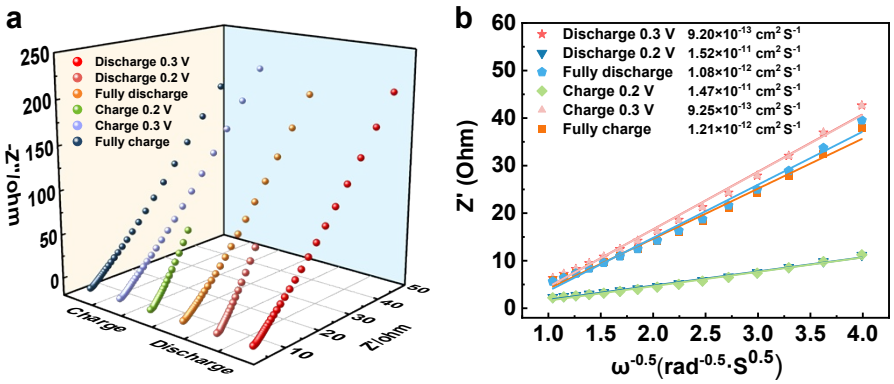

Figure S8. (a) EIS of the TTA electrode at various potential during a typical GCD cycles. (b) The relationship between the Z′ and $\omega^{-1/2}$, along with the calculated D values.

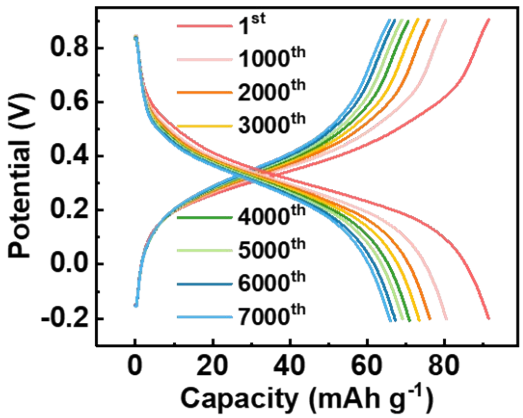

Figure S9. GCD curves of the TTA electrode with different cycles.

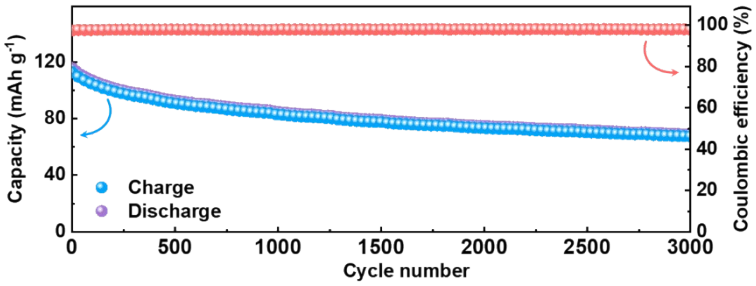

Figure S10. Cycle performance of the TTA electrode at 0.5 A g^{-1}.

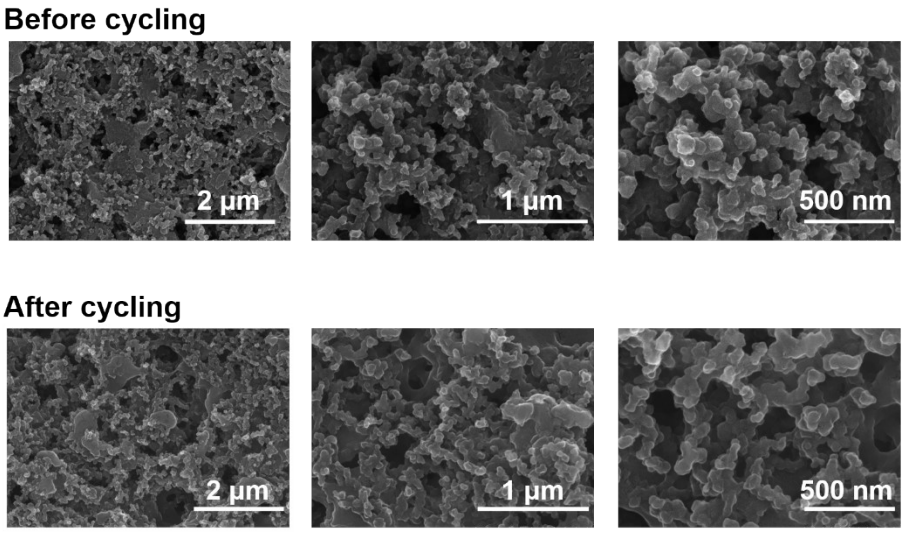

Figure S11. SEM images with different magnifications of the TTA electrodes before and after cycling.

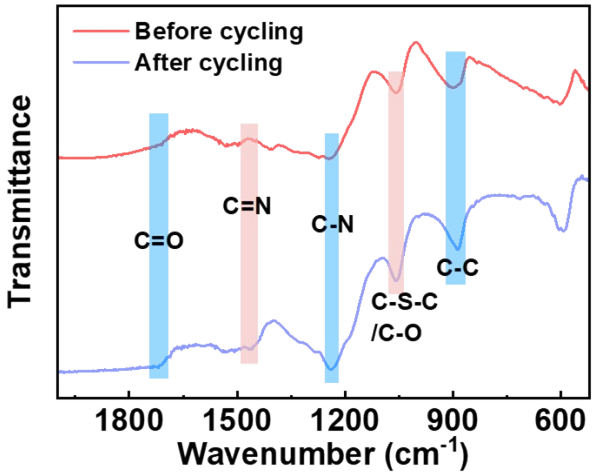

Figure S12. FTIR spectra of the TTA electrodes before and after cycling.

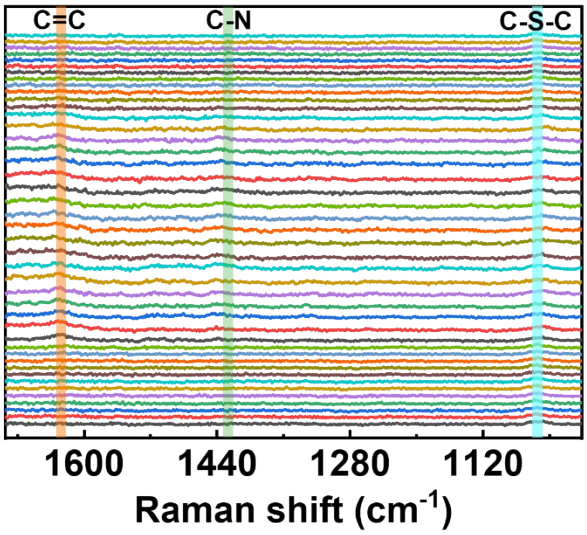

Figure S13. In-situ Raman spectra of the TTA electrode in H_2SO_4 electrolyte.

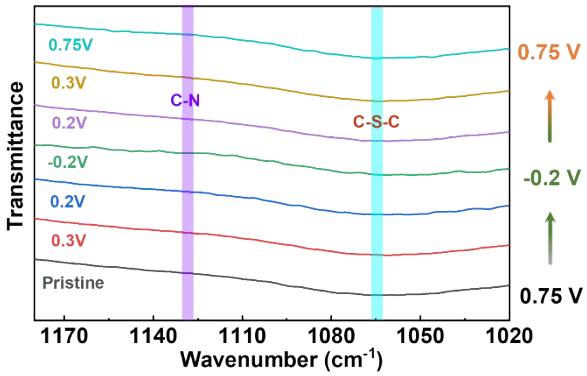

Figure S14. Ex-situ FTIR spectra of TTA electrode. The peak at 1062 cm^{-1} is ascribed to C-S-C asymmetric vibration.

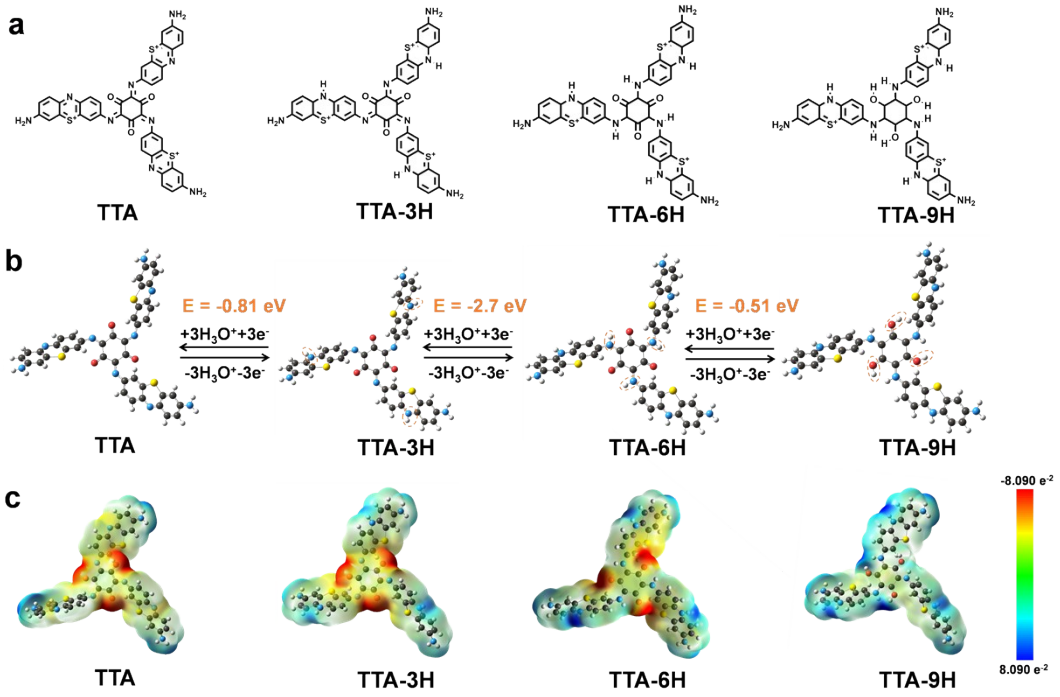

Figure S15. Calculated reaction pathways of TTA. (a) Chemical structures of TTA and the corresponding reaction intermediate molecules. (b) The possible redox routes of TTA. (c) Electrostatic potential mapping of TTA and intermediate molecules.

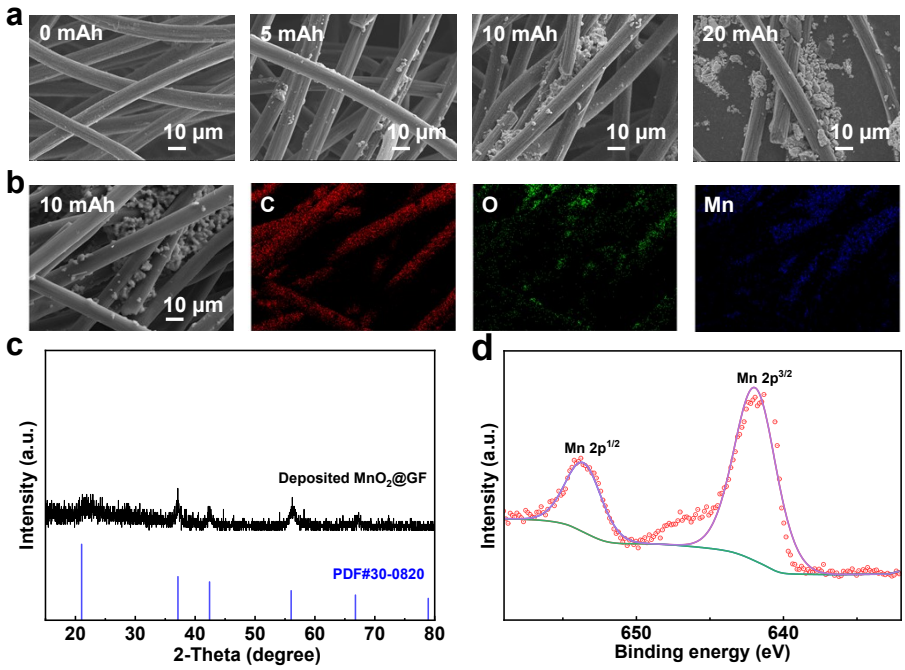

Figure S16. (a) SEM images of MnO_2 deposited on GF with different deposition capacities (0 mAh, 2 mAh, 5 mAh, and 10 mAh). (b) EDS images of C, O and Mn. (c) XRD pattern of the deposited MnO_2@GF electrode. (d) XPS spectra of Mn element after deposition.

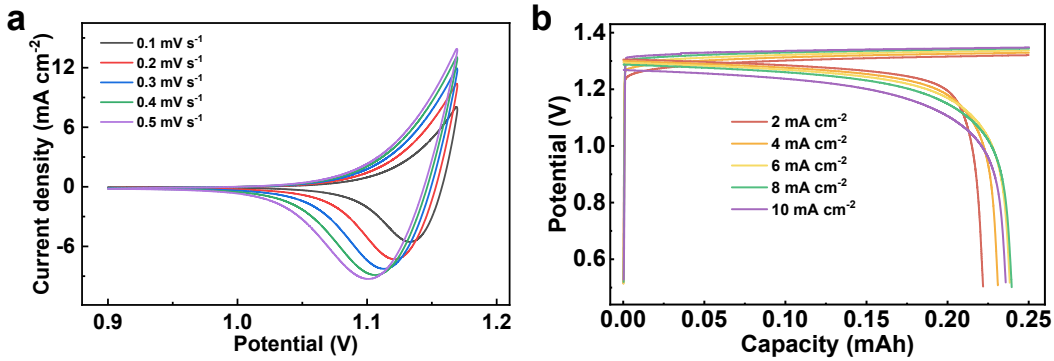

Figure S17. (a) CV profiles of the GF electrode measured at various scan rates. (b) GCD curves of the GF electrode.

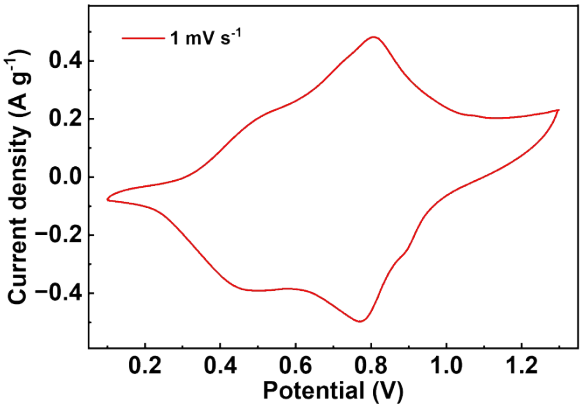

Figure S18. CV curve of full cells at 1 mV s^{-1}.

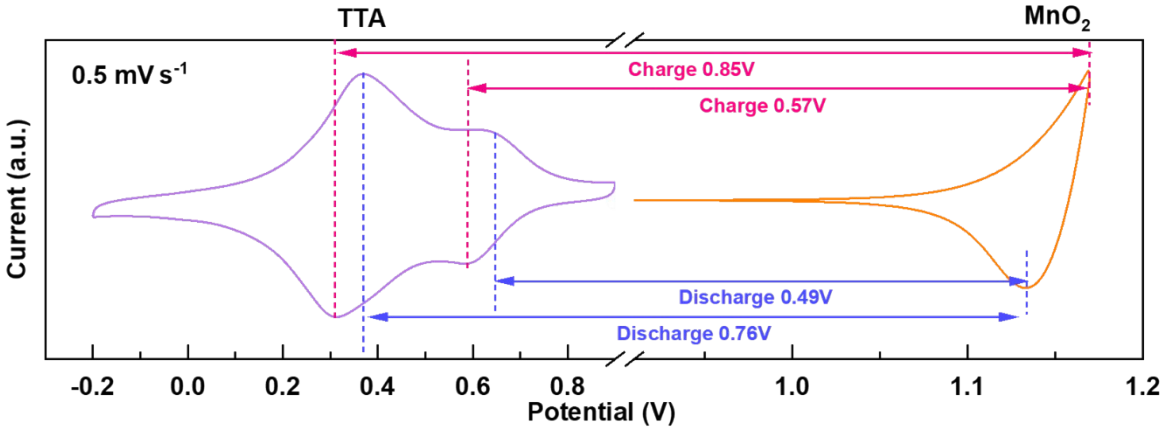

Figure S19. Comparison of CV profiles for the TTA electrode and MnO_2 electrode at the same scan rate of 0.5 mV s^{-1}.

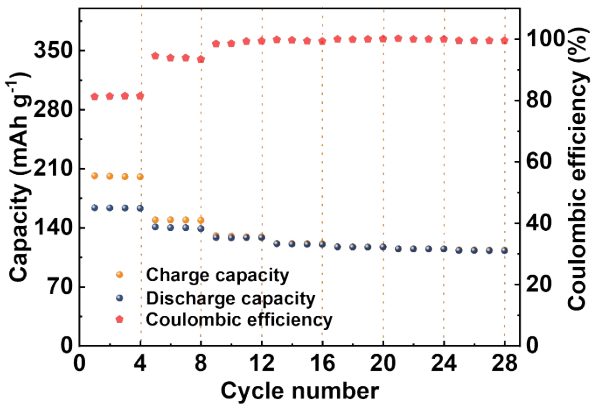

Figure 20. Rate perforamnce of the full cells.

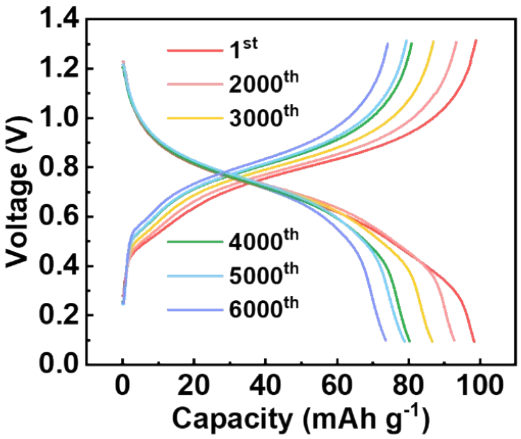

Figure S21. GCD curves of the full cells with different cycles.

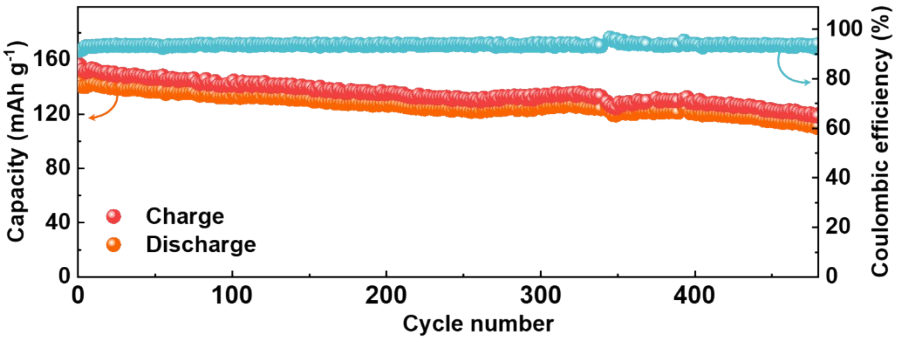

Figure S22. Cycle performance of the full cells at 0.5 A g^{-1}.

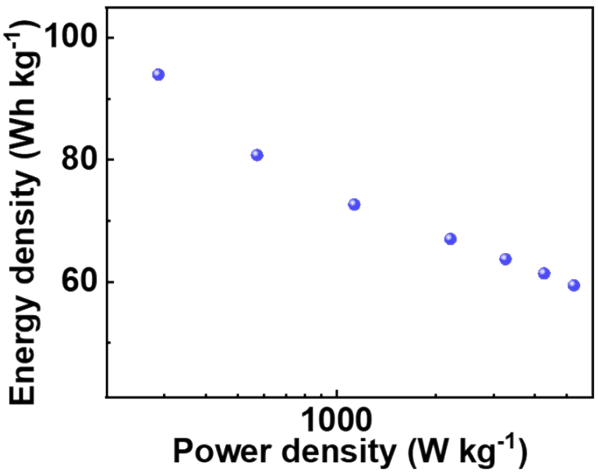

Figure S23. Ragon plot of the full cells.

Table S1. Performance comparison of several electrode materials for H_3O^+ storage and battery systems.

Refs.	Anode	Cathode	Cycling stability of full cell (Capacity retention%)
1	PTO	PbO_2	1500 (96% at 0.8 A g^{-1})
2	PTO	MnO_2	5000 (62% from 20th to 5000th at 2 mA cm^{-2})
3	ALO	MnO_2	300 (~67% at 5 A g^{-1})
4	CuFe-TBA	MoO_3	1000 (85% at 2 A g^{-1})
5	PI	MnO_2	5000 (68.0% at 5 A g^{-1})
6	HATN	MnO_2	500 (92.6% at 1 A g^{-1})
7	TMBQ	MnO_2	4000 (77% at 5 C)
8	DHAQ	MnO_2	2600 (60.0% at 1.13 A g^{-1})
This work	TTA	MnO_2	6000 (72% at 10 A g^{-1})

1. Y. Liang, Y. Jing, S. Gheytani, K.-Y. Lee, P. Liu, A. Facchetti and Y. Yao, *Nat. Mater.*, 2017, **16**, 841-848.
2. Z. Guo, J. Huang, X. Dong, Y. Xia, L. Yan, Z. Wang and Y. Wang, *Nat. Commun.*, 2020, **11**, 959.
3. T. Sun, H. Du, S. Zheng, J. Shi and Z. Tao, *Adv. Funct. Mater.*, 2021, **31**, 2010127.
4. Y.-H. Chen, H.-T. Guo, B.-C. Liu, J. Li, Z.-L. Liu, P.-F. Wang, Y.-R. Zhu and T.-F. Yi, *J. Colloid Interface Sci.*, 2025, **690**, 137342.
5. Z. Wu, P. Yang, S. Wang, S. Li and S. Zhang, *Trends in Chem.*, 2022, **4**, 1121-1134.
6. Y. Dai, X. Yan, J. Zhang, C. Wu, Q. Guo, J. Luo, M. Hu and J. Yang, *Electrochim. Acta*, 2023, **442**, 141870.
7. X. Yang, Y. Ni, Y. Lu, Q. Zhang, J. Hou, G. Yang, X. Liu, W. Xie, Z. Yan, Q. Zhao and J. Chen, *Angew. Chem. Int. Ed.*, 2022, **61**, e202209642.
8. J. Yu, J. Li, Z. Y. Leong, D.-s. Li, J. Lu, Q. Wang and H. Y. Yang, *Mater. Today Energy*, 2021, **22**, 100872.